ARTICLE   OPEN

Check for updates

Strong quartic anharmonicity, ultralow thermal conductivity, high band degeneracy and good thermoelectric performance in Na$_2$TlSb

Tongcai Yue[1], Yinchang Zhao[1 ✉], Jun Ni[2 ✉], Sheng Meng[3,4 ✉] and Zhenhong Dai[1 ✉]

We employ first-principles calculations combined with self-consistent phonon theory and Boltzmann transport equations to investigate the thermal transport and thermoelectric properties of full-Heusler compound Na$_2$TlSb. Our findings exhibit that the strong quartic anharmonicity and temperature dependence of the Tl atom with rattling behavior plays an important role in the lattice stability of Na$_2$TlSb. We find that soft Tl-Sb bonding and resonant bonding in the pseudocage composed of the Na and Sb atoms interaction is responsible for ultralow κ_L. Meanwhile, the multi-valley band structure increases the band degeneracy, results in a high power factor in p-type Na$_2$TlSb. The coexistence of ultralow κ_L and high power factor presents that Na$_2$TlSb is a potential candidate for thermoelectric applications. Moreover, these findings help to understand the origin of ultralow κ_L of full-Heusler compounds with strong quartic anharmonicity, leading to the rational design of full-Heusler compounds with high thermoelectric performance.

INTRODUCTION

Thermoelectric (TE) materials are capable of converting heat energy into electricity without additional pollution, promising to alleviate the energy shortage and environmental pollution caused by energy use[1–3]. Conventionally, the conversion efficiency of TE materials is measured by the figure of merit $zT = \frac{S^2 \sigma T}{\kappa_e + \kappa_L}$, in which S, σ, κ_e, κ_L, and T are the thermopower, electrical conductivity, electrical thermal conductivity, lattice thermal conductivity, and absolute temperature, respectively. In principle, high-efficiency TE materials need to possess both a high TE power factor (PF $= S^2 \sigma$) and low thermal conductivities ($\kappa = \kappa_e + \kappa_L$). The former involves band tuning[4,5], applying strain[6], and doping[7,8]. Meanwhile, to capture an inherently high PF, the anisotropic electronic bands and multi-valley band structure have been proposed[9–13], in which the dispersive part leads to high σ and carrier mobility μ, while the flat (multi-valley) part induces large S. However, due to the mutual coupling of S and σ, it is difficult to improve the zT value by tuning a single parameter. To address this problem, common strategies are to suppress the κ_L of existing TE materials through introducing defects[14,15], alloying[16,17], nanostructures[18], and substructures[19,20], or to search for TE materials with inherently low κ_L.

Recently, high zT values of a series of full-Heusler compounds have been reported, such as Ba$_2$BiAu[21], Sr$_2$SbAu[22], Ca$_2$HgPb[23], and Ba$_2$AgSb[24], which is mainly attributed to the ultralow κ_L. Particularly, a very high zT value of 5 has been reported in full-Heusler compounds Ba$_2$BiAu[21]. Hence, understanding the lattice dynamic behavior and phonon thermal transport in full-Heusler compounds is critical to gain insights into which can further suppress κ_L and enhance zT. However, existing theoretical studies only focus on full-Heusler compounds with lattice stability (no imaginary phonon frequencies) at 0 K. However, many materials with ferroelectric-like lattice instability also have good TE properties, such as Rb$_3$AuO[25], SnSe[26], Cu$_2$Se[27], and GeTe[16,28]. However,

the comprehensive understanding of full-Heusler compounds is hampered by the existence of imaginary phonon frequencies and the failure to consider higher-order anharmonic effects. Especially for some TE materials with imaginary phonon frequencies, the four-phonon (4ph) scattering processes even exceed three-phonon (3ph) scattering processes[16,29,30].

In view of the above, we perform fist-principles calculations, self-consistent phonon (SCP) theory, and Boltzmann transport equations to investigate the thermal transport and TE properties in full-Heusler compound Na$_2$TlSb. We consider the contribution of quartic anharmonic renormalization of phonon frequencies to phonon group velocity v_{ph} as well as the influence of 3ph and 4ph scattering to the phonon lifetimes τ_{ph}. The phonon spectrum, thermal conductivity spectrum κ_L (ω_{ph}), 3ph and 4ph scattering processes, etc. are investigated to uncover the microscopic mechanism of thermal transport. Our key finding is that a rational κ_L and temperature dependence can be obtained by including full quartic anharmonicity. Meantime, the ultralow κ_L is captured in Na$_2$TlSb due to the soft Tl-Sb bonding and resonant bonding in the pseudocage composed of the Na and Sb atoms interaction. Additionally, the multi-valley band structure increases the band degeneracy, resulting in a high PF in Na$_2$TlSb. High PF combined with ultralow κ_L means good TE performance, with the highest zT values of 2.88 (0.94) at 300 K in p-type (n-type) full-Heusler compound Na$_2$TlSb.

RESULTS

Structural stability

Na$_2$TlSb crystallizes in the face-centered cubic structure (space group Fm$\bar{3}$m [225]), where Na, Tl, and Sb take up the 8c, 4a, and 4b sites, respectively, as shown in Fig. 1d. The calculated lattice constants of the crystal cell is 7.485 Å, and the bond length of Na-

[1]Department of Physics, Yantai University, Yantai 264005, P. R. China. [2]Department of Physics, Tsinghua University, Beijing 100084, P. R. China. [3]Beijing National Laboratory for Condensed Matter Physics and Institute of Physics, Chinese Academy of Sciences, Beijing 100190, P. R. China. [4]Collaborative Innovation Center of Quantum Matter, Beijing 100084, P. R. China. ✉email: y.zhao@ytu.edu.cn; junni@mail.tsinghua.edu.cn; smeng@iphy.ac.cn; zhdai@ytu.edu.cn
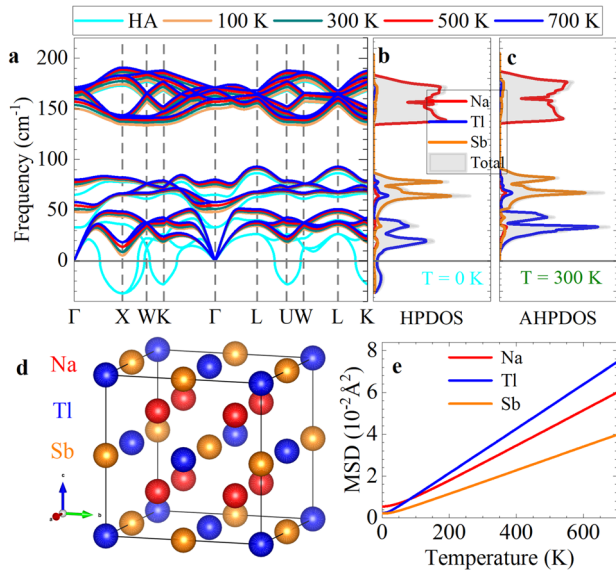
Fig. 1 Lattice vibration properties. a The temperature-dependent phonon spectrum from $T = 0$ to 700 K for Na$_2$TlSb. The cyan line denotes the HA phonon dispersion ($T = 0$ K), and the orange, dark cyan, red, and blue lines represent the SCP dispersion at 100, 300, 500, and 700 K, respectively. **b, c** The element-decomposed and total phonon density of states (PDOS) at $T = 0$ and 300 K, respectively. **d** The crystal structure of Na$_2$TlSb, as visualized in VESTA code[62]. The red, blue, and orange balls denote Na, Tl, and Sb atoms, respectively. **e** The temperature-dependent atomic mean square displacements (MSDs) from 100 to 700 K along the [100] direction. The MSD from 100 to 700 K are the result of the SCP approximations.

Sb/Tl (Tl-Sb) is 3.241 (3.743) Å. The dielectric tensors ϵ and Born effective charges Z^* are listed in Supplementary Table 1. To investigate the dynamics stability, we calculated the HA and anharmonic phonon dispersion curves of Na$_2$TlSb, as shown in Fig. 1a. In HA approximations, the imaginary frequencies indicate that Na$_2$TlSb is dynamically unstable at 0 K. However, after considering the renormalization of phonon frequencies by the quartic anharmonicity, the imaginary frequencies disappear, indicating that Na$_2$TlSb is dynamics stable between 100 and 700 K. Furthermore, as shown in Supplementary Fig. 6, Na$_2$TlSb is on the convex hull in the ternary phase diagram, which indicates it is the minimum free energy structure under this component. Hence, the full-Heusler compound Na$_2$TlSb is most likely to be experimentally synthesized to form a stable structure. Additionally, a 20,000-step AIMD is simulated to estimate the stability of Na$_2$TlSb at high temperatures, as shown in Supplementary Fig. 1. There is no significant change in free energy, indicating that Na$_2$TlSb is stable at 700 K. Furthermore, the mechanical stability is also estimated, and the elastic constants are list in Supplementary Table 1. Na$_2$TlSb meets the mechanical stability criteria of the cubic lattice structure, as written in

$$C_{11} - C_{12} > 0, \qquad C_{11} + 2C_{12} > 0, \qquad C_{44} > 0, \qquad (1)$$

indicating Na$_2$TlSb is mechanically stable[31].

Phonon transport

For strongly anharmonic materials, quartic anharmonicity needs to be considered to obtain reasonable κ_L and temperature dependence[32]. First, we investigate the impact of quartic anharmonicity on phonon frequencies ω_{ph}. We find that the phonon modes below 50 cm^{-1} shift up significantly with increasing temperature,
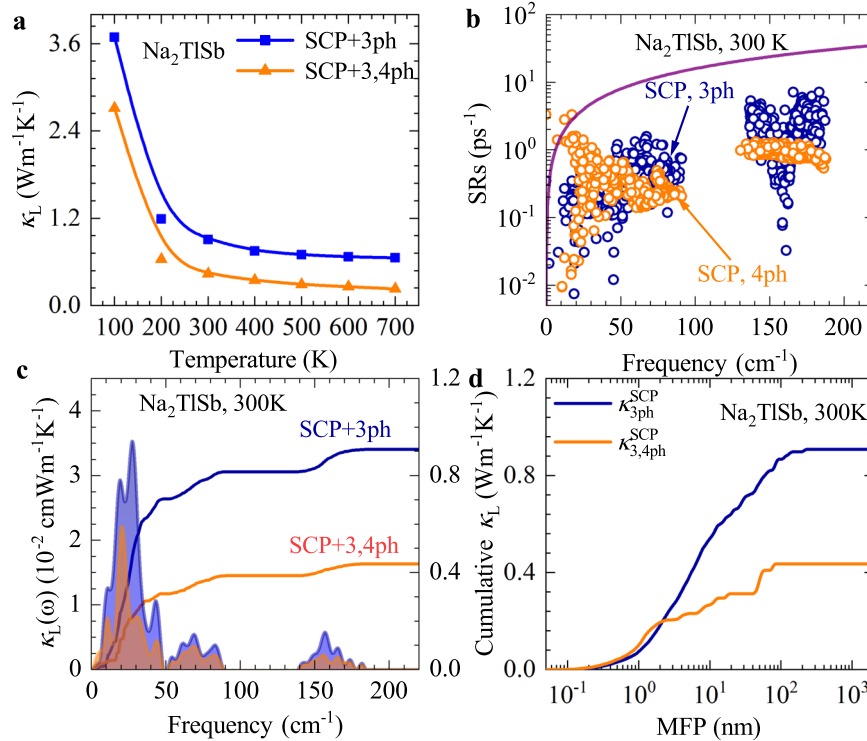

Fig. 2 Phonon transport properties. a The calculated temperature-dependent κ_L from 100 to 700 K by using SCP+3ph and SCP+3,4ph, respectively. **b** The calculated 3ph (blue empty circles) and 4ph (orange empty circles) scattering rates (SRs) in the SCP approximations. The purple line denotes $1/\tau_{ph} = \omega_{ph}/2\pi$, that is, the scattering rates equal to phonon frequencies. **c** The κ_L spectrum (The filled area below the lines) and cumulative κ_L at 300 K by using SCP+3ph and SCP+3,4ph, respectively. **d** Same as **c** but for the maximum mean free path (MFP) cumulative κ_L at 300 K.
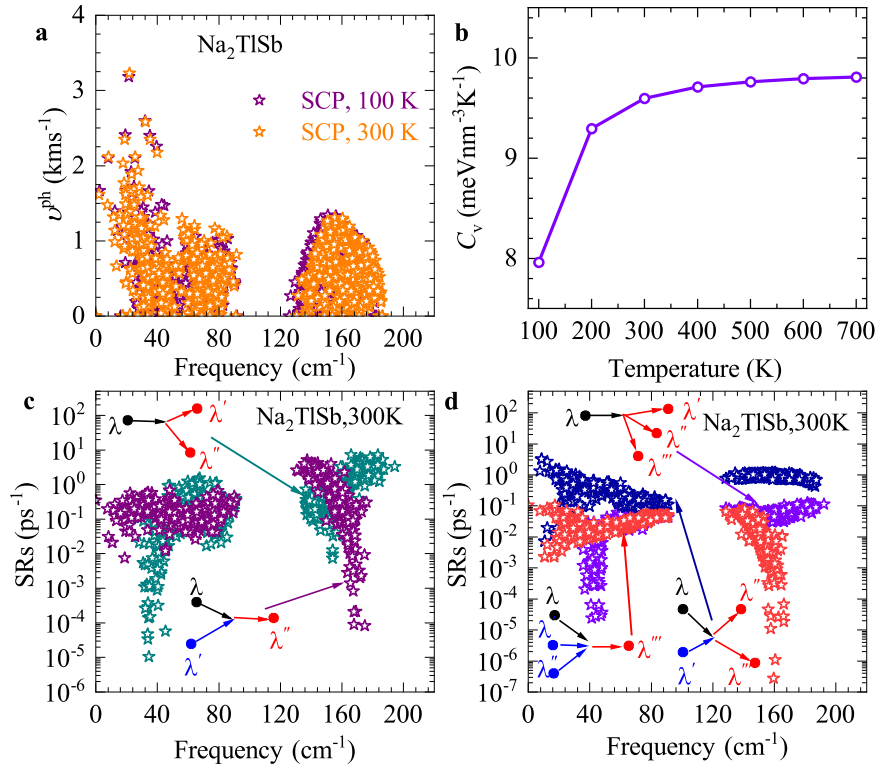
Fig. 3 Phonon transport parameter. a The phonon group velocity v_{ph} at 100 and 300 K. **b** The calculated specific heats C_V. **c** Decomposed 3ph scattering rates into the slitting ($\lambda \rightarrow \lambda' + \lambda''$) and combination ($\lambda + \lambda' \rightarrow \lambda''$) processes at 300 K. **d** Decomposed 4ph scattering rates into the splitting ($\lambda \rightarrow \lambda' + \lambda'' + \lambda'''$), redistribution ($\lambda + \lambda' \rightarrow \lambda'' + \lambda'''$), and combination ($\lambda + \lambda' + \lambda'' \rightarrow \lambda'''$) processes at 300 K. All of the above results were obtained using SCP method.

as shown in Fig. 1a. Figure 1b, c reveal that the vibrations of Tl atoms dominate these phonon modes with imaginary frequencies. While the optical phonon branches, mainly contributed by the vibrations of Sb and Na atoms, is shifted upward only slightly. The vibrational behavior associated with the Tl atom is similar to that of the rattling modes in clathrates and skutterudites, whose phonon frequencies exhibit small values and strong temperature dependence[33]. Actually, avoiding the overlap of acoustic and optical phonon modes is a clear sign of the rattling behavior of Tl atoms[34]. The large mean square displacements (MSDs) and weak bonding of Tl atoms also confirm the above conclusion, as shown in Figs. 1e and 5b. Additionally, the phonon frequency shifts caused by cubic anharmonicity is not included in our calculations. Generally, the frequency shifts due to cubic anharmonicity is negative ($\Delta\omega_q < 0$) and much smaller than the frequency hardening induced by quartic anharmonicity[33]. If the frequency shifts caused by cubic anharmonicity is considered, the hardening of low-lying phonon mode will be slightly suppressed, resulting in a slight decrease in the κ_L.

The imaginary HA phonon frequency will induce the phase transition of Na$_2$TlSb at low temperatures. To predict the phase transition temperature T_c of Na$_2$TlSb, we also calculated the temperature dependence of the squared frequency of the lowest acoustic phonon mode at X point, which is the softest mode in the region away from the Brillouin zone center, as shown in Supplementary Fig. 4. Above approximately room temperature, the temperature dependence of squared frequency can be rationally fitted by equation $\Omega_q(T) = a(T - T_c)^2$[35], where T_c is the phase transition temperature. Applying the above equation, we obtain the phase transition temperature T_c as 83 K.

We calculate the temperature-dependence lattice thermal conductivities κ_{3ph}^{SCP} and $\kappa_{3,4ph}^{SCP}$ from 100 to 700 K for Na$_2$TlSb, as plotted in Fig. 2a. Due to the existence of imaginary frequencies,

the solution of κ_L under HA approximations is numerically invalid. Hence, only the κ_L results of SCP approximations are provided. Compared with κ_{3ph}^{SCP}, $\kappa_{3,4ph}^{SCP}$ is significantly reduced due to the effect of 4ph scatterings. The calculated κ_{3ph}^{SCP} and $\kappa_{3,4ph}^{SCP}$ are 0.91 and 0.44 Wm^{-1} K^{-1} at 300 K for Na$_2$TlSb, respectively. The values of $\kappa_{3,4ph}^{SCP}$ is ultralow, half that of quartz glass (κ_L ~0.9 WK^{-1} m^{-1}). To further explore the microscopic mechanism of heat conduction, we use the $\kappa_L \sim T^{-\alpha}$ to analysis the temperature dependence of κ_L. We evaluated the temperature dependence of κ_L from 200 to 700 K, since κ_L at extremely low temperature is mainly determined by the lattice-specific heat C_V following the Debye T^3 law[29]. The κ_{3ph}^{SCP} exhibits anomalously temperature dependence, $\kappa_{3ph}^{SCP} \sim T^{-0.52}$, which deviates far from the universal law $\kappa_L \sim T^{-1}$. By including 4ph scattering, the temperature dependence of the $\kappa_{3,4ph}^{SCP}$ is enhanced and the value of α becomes 0.84. The increased temperature dependence of $\kappa_{3,4ph}^{SCP}$ further confirms the importance of the quartic anharmonicity for the materials with imaginary frequencies. Additionally, thermal expansion and additional phonon-grain boundary scattering also play a crucial role in determining κ_L and corresponding temperature dependence[32,36]. If the above factors are taken into account when estimating the phonon thermal transport properties, κ_L will decrease and temperature dependence of κ_L will be closer to the experimental results. Furthermore, we verify the feasibility of excluding the thermal expansion and cubic anharmonicity, we calculated the $\kappa_{3,4ph}^{SCP}$ considering the thermal expansion and discussed the effect of the cubic anharmonicity on the phonon frequencies. As shown in Supplementary Figs. 7, 8, $\kappa_{3,4ph}^{SCP}$ considering thermal expansion at 700 K is 4.1% lower than that without considering thermal expansion. Moreover, we observe that the phonon frequency shift caused by cubic anharmonicity at X point is very small, only 4.21 cm^{-1} at 700 K, and this value will
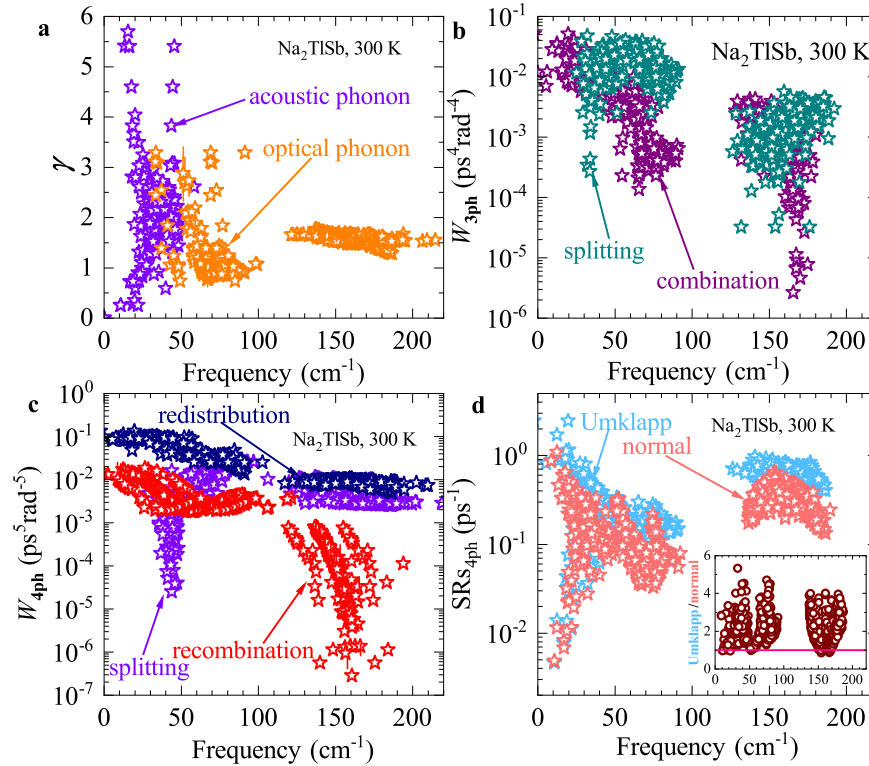
Fig. 4 Phonon scattering. a The Grüneisen parameter γ of acoustic (violet) and optical (orange) phonon branches. **b** The decomposed 3ph scattering phase space W_{3ph} into the splitting and combination processes. **c** The decomposed 4ph scattering phase space W_{4ph} into the splitting, redistribution, and combination processes. **d** Decomposed 4ph scattering rates into the normal and Umklapp processes. The inset represents the ratios between Umklapp and normal processes.

not significantly change the phonon spectrum. Hence, it is rational to exclude the above factors to calculate κ_L.

The large 3ph and 4ph SRs are one of the main reasons for the ultralow κ_L of Na$_2$TlSb, as shown in Fig. 2b. Similar to 3ph scattering, 4ph scattering is also important in phonon thermal transport. It is evident from the calculations that 4ph SRs even exceeds 3ph SRs below 50 cm^{-1}. The strong 4ph SRs can be attributed to the strict constraints on the 3ph scattering phase space by the selection rule[37]. Similar to BAs, the 3ph scattering phase spaces are restricted by the selection rule due to the large phonon band gap, resulting in a weakened 3ph SRs in Na$_2$TlSb. Meantime, the selection rule has little effect on the 4ph scattering phase spaces, resulting in large 4ph SRs. The SRs curve equal phonon frequencies is also plotted by the purple line in Fig. 2b, which means that the phonon lifetime τ_{ph} is equal to the vibrational period of the phonon quasiparticle. The phonon quasiparticle image is invalid if the τ_{ph} is less than one vibrational period, i.e., the phonon annihilates before completing one vibration[29]. As shown in Fig. 2b, all 3ph and most 4ph scattering distributions are below the curve, indicating that our BTE scheme is valid. The κ_L spectrum and frequency cumulative κ_L indicate that the major contributions to the κ_L are the phonon branches below 50 cm^{-1}. Meantime, the phonon branches below 50 cm^{-1} are the major contributions to the suppressed κ_L calculated with SCP +3,4ph relative to SCP+3ph, which is consistent with strong 4ph SRs below 50 cm^{-1}. Figure 2d show the cumulative κ_L as the function of maximum MFP. The result shows that heat-carrying phonons have considerable MFPs at 300 K. The maximum MFP of κ_{3ph}^{SCP} is about 210 nm, while the maximum MFP of $\kappa_{3,4ph}^{SCP}$ is only about 80 nm. Through nanostructuring, the $\kappa_{3,4ph}^{SCP}$ can be lower, e.g., as low as 0.27 WK^{-1} m^{-1} when the maximum MFP is limited to 10 nm.

The phonon group velocity v_{ph} at 100 and 300 K is shown in Fig. 3a. The small v_{ph} further confirms the ultralow κ_L of Na$_2$TlSb. Relative to 100 K, the v_{ph} of 300 K is slightly larger below 50 cm^{-1}, which is consistent with the change of the phonon dispersion curves form 100 to 300 K. The observed small specific heats C_V further indicates the existence of ultralow κ_L, as shown in Fig. 3b. Figure 3c show the decomposed 3ph scattering rate. The combination (splitting) processes dominate the low-frequency (high-frequency) 3ph SRs below 100 cm^{-1}. Due to the large phonon band gap from 100 to 130 cm^{-1}, it is difficult for low-frequency phonon modes to be excited to high-frequency phonon modes through the combination processes. To obey the energy conservation constraint, high-frequency phonons can only be generated by the three-phonon scattering process of high-frequency phonons. Hence, the 3ph SRs of high-frequency phonons exhibit the same regularity as those of low-frequency phonons, e.g., the 3ph SRs of low-frequency (high-frequency) modes above 130 cm^{-1} are mainly determined by the combination (splitting) processes. Figure 3d show the decomposed 4ph scattering rates. The redistribution processes dominate the 4ph scattering processes because it is easier to satisfy the selection rule[37]. With respect to the 4ph scattering processes, due to the strong redistribution processes, the splitting processes at low frequencies is suppressed and weaker than the combination processes. It is only at very high phonon frequencies that the splitting processes are larger than the combination processes.

To further understand the microscope mechanism of the ultralow κ_L, we calculated the Grüneisen parameter γ and 3ph scattering phase space W_{3ph}, as shown in Fig. 4a, b. Compared with the optical phonon modes, the acoustic phonon modes have larger γ, indicating that the acoustic phonon modes have stronger cubic anharmonicity. This result is consistent with our previous analysis that the rattling behavior of Tl atoms have stronger
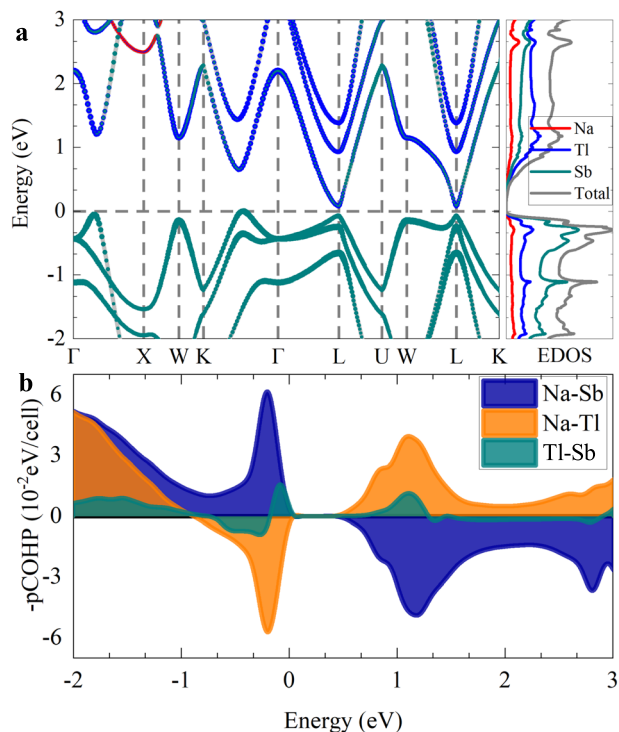
Fig. 5 Electron structure. a The projected electronic structure and partial electronic density of states for Na$_2$TlSb using the PBEsol functional. **b** The calculated projected crystal orbital Hamilton population (pCOHP) analysis for the Na-Sb, Na-Tl, and Tl-Sb of Na$_2$TlSb. The negative values of pCOHP present antibonding states. The Fermi energy level is put in 0 eV.

anharmonicity. Figure 4b, c show the large 3ph and 4ph scattering phase spaces, indicating that Na$_2$TlSb have large anharmonic scattering rates. Meanwhile, The decomposed anharmonic (3ph and 4ph) scattering phase spaces exhibit a similar law to the decomposed anharmonic scattering rates. Figure 4d show the decomposed 4ph SRs into normal and Umklapp processes. The Umklapp processes dominate the 4ph SRs of the entire phonon modes, indicating that the 4ph scattering processes mainly suppress heat conduction, which is consistent with the above analysis of κ_L. The Umklapp processes are much larger than the normal processes, which also confirms the above analysis, as shown in the inset of Fig. 4d.

Electronic structure

Figure 5a show the electronic band structure and density of states (DOS) of Na$_2$TlSb. Na$_2$TlSb is an indirect band gap semiconductor with the conduction band minimum (CBM) at the L point and the valence band maximum at the $K - \Gamma$ high symmetry line. The calculated band gap is 0.08 eV using the PBEsol functional with SOC, which is in the range commonly found in TE materials. In Na$_2$TlSb, the CBM is mainly contributed by Sb and Tl atoms, while the VBM is almost entirely contributed by Sb atoms. The CBM has high electronic band dispersion, which will lead to high electrical conductivity σ. Meantime, the observed remarkable band asymmetry at CBM further manifests a good TE performance in n-type Na$_2$TlSb[38]. A multi-valley band structure at VBM results in high degeneracy. Additionally, the second ($\Gamma - X$ line) and third (W point) highest valleys of the valence band are very close to the VBM, by doping, we can achieve a higher degeneracy. A large degree of degeneracy means that p-type Na$_2$TlSb has a high Seebeck coefficient S. Meanwhile, multiple valleys create additional conduction channels, resulting in high σ. Figure 5b show the projected crystal orbital Hamilton population (pCOHP) analysis. At the VBM, Na$-$Sb and Tl$-$Sb show bonding states, while Na$-$Tl
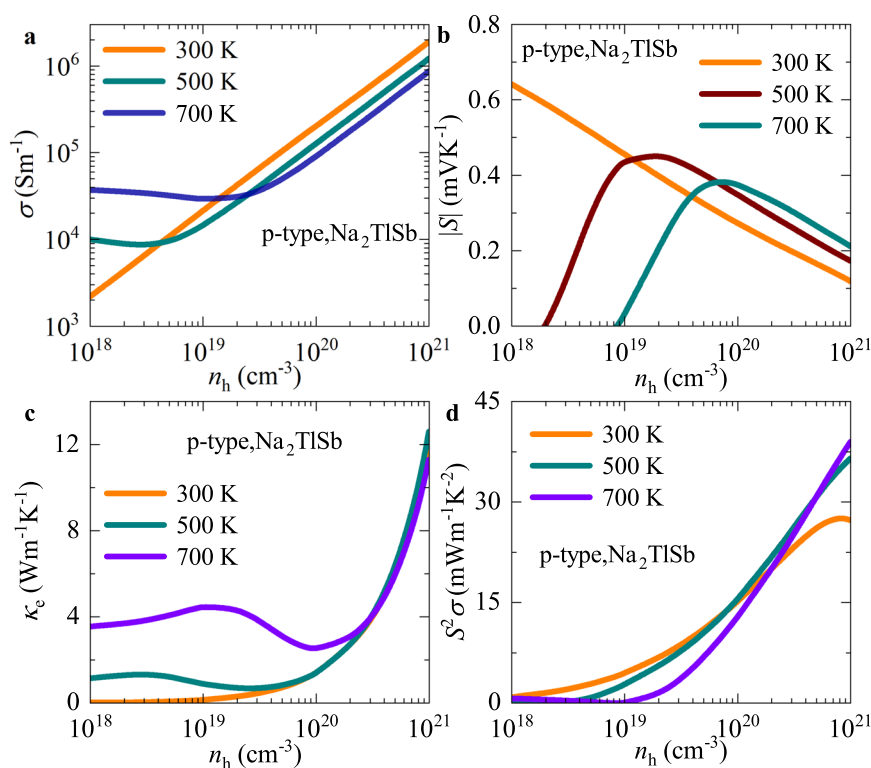

Fig. 6 Electronic transport parameters. The calculated electronic transport parameters for p-type Na$_2$TlSb at 300, 500, and 700 K. **a** Electrical conductivity σ. **b** The Seebeck coefficient $|S|$. **c** The electronic thermal conductivity κ_e. **d** TE power factor. The SOC is also included in the calculations.
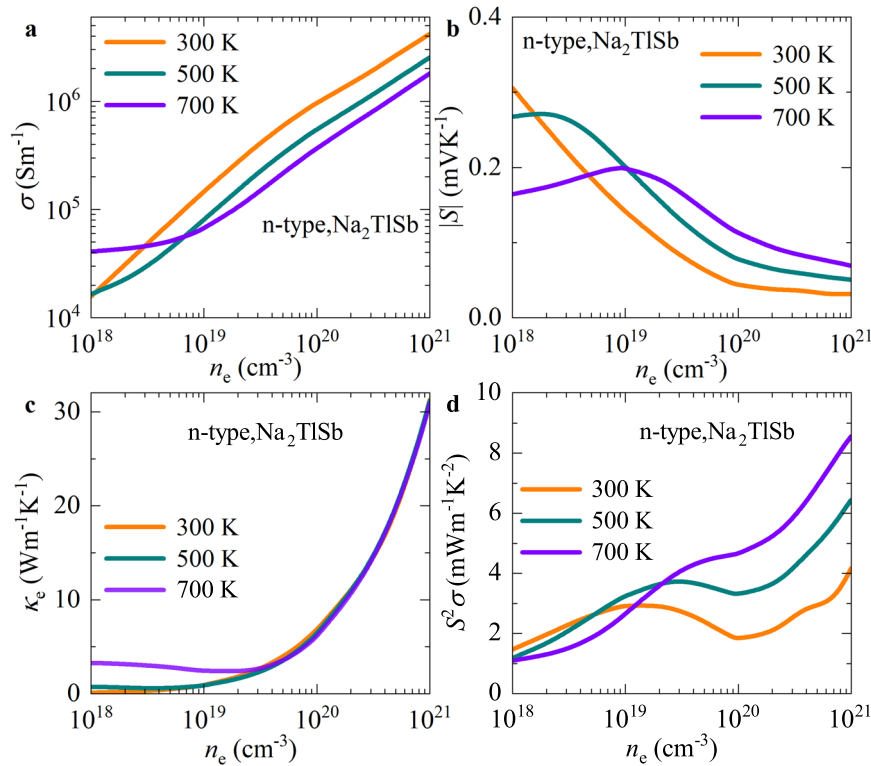
Fig. 7 Electronic transport parameters. The calculated electronic transport parameters for n-type Na$_2$TlSb at 300, 500, and 700 K, respectively. **a** Electrical conductivity σ. **b** The Seebeck coefficient $|S|$. **c** The electronic thermal conductivity κ_e. **d** TE power factor. The SOC is also included in the calculations.

presents antibonding states. Obviously, the Tl atoms are weakly bound to other atoms, which is consistent with the MSD results.

Since the band gap of materials is usually underestimated using PBE functional, we recalculated the band gap accurately with HSE06 functional with SOC, as shown in Supplementary Fig. 2. The band gap of HSE06 functional with SOC is 0.30 eV. Since the electronic structures of HSE06 and PBEsol functional are not obviously different except for the band gap for Na$_2$TlSb, the band gap of the HSE06 functional is used to obtain rational electronic transport properties. The carrier relaxation time τ of Na$_2$TlSb is calculated by considering the ADP, IMP, and POP scattering mechanisms, as shown in Supplementary Fig. 3.

Electron transport

Figures 6, 7 show the electronic transport parameters for p-type and n-type Na$_2$TlSb, respectively. We observe that σ is proportional to carrier concentration n and inversely proportional to temperature T. The former is due to an increase in the number of carriers participating in the conduction process due to an increase in the concentration n. The latter is attributed to the increased scattering rates dominated by the electron-phonon interaction caused by the temperature increase, which is consistent with the results in Supplementary Fig. 3. The n-type Na$_2$TlSb exhibits higher σ relative to the p-type Na$_2$TlSb, which is consistent with our previous analysis of the larger electronic band dispersion at the CBM. Unlike σ, the S decreases with increasing n at the same T, while the S increases with increasing T at the same n. Apparently, p-type Na$_2$TlSb exhibits a large S due to the large degeneracy at the VBM. In general, κ_e and σ vary in the same law with n due to the increase in heat carrier, which is consistent with the trend in Fig. 6c and d. Due to the coexistence of a large S and σ, we obtain a high TE power factor. Particularly, S have single peak at 500 and 700 K due to the bipolar effect[39]. The above phenomenon is also observed in PbTe and PbSe with small band gaps[40,41]. The strong

bipolar effect severely suppresses the S, leading to a decrease in TE performance. As a result, the highest PF is obtained at 500 K because the bipolar effect increases with temperature. At the optimal doping concentration n, the power factor is 2.26 (2.92) m Wm^{-1} K^{-2} for n-type Na$_2$TlSb at 300 (500) K. Due to the multi-valley structure at the VBM, p-type Na$_2$TlSb has a large power factor, e.g., 9.84 and 12.76 mW m^{-1} K^{-2} at 300 and 500 K, respectively. Moreover, the strong quartic anharmonicity of Na$_2$TlSb affects not only phonon thermal transport properties but also electronic transport properties. Concretely, strong quartic anharmonicity leads to a hardening of phonon frequency, thereby reducing the electron-phonon coupling strength. Furthermore, the reduced electron-phonon coupling strength results in higher carrier mobility and larger electrical conductivity[42]. Hence, if the influence of quartic anharmonicity on electronic transport is included, the TE performance of Na$_2$TlSb will be further improved.

The combination of ultralow κ_L and high TE power factor in the Na$_2$TlSb captures an anomalously high $zT \sim 4.81$ for hole doping at $n_h \sim 7 \times 10^{19}$ cm^{-3} and 500 K, as shown in Fig. 8a. Meanwhile, we predict the $zT \sim 2.88$ at $n_h \sim 4 \times 10^{19}$ cm^{-3} and 300 K, which is also ultrahigh value for almost TE materials at room temperature. Due to the existing of large electronic band dispersion and remarkable band asymmetry at CBM, the zT is also very high for n-type Na$_2$TlSb, e.g., 0.94 (1.48) at $n_e \sim 3 \times 10^{18}$ (7×10^{18}) cm^{-3} and 300 (500) K, as shown in Fig. 8b. The optimum n_e for n-type Na$_2$TlSb is far small related to n_h in the p-type case, which means that n-type case is easier to achieve good TE performance. Hence, we also recommend n-type Na$_2$TlSb as a potential TE material. Additionally, the zT value calculated based on the result of κ_{3ph}^{SCP} is also given as the lower limit. Nonetheless, Na$_2$TlSb also exhibits good TE properties, e.g., 1.05 (3.72) for n-type (p-type) case at 500 K. Additionally, thermal radiation[43], air-induced thermal convection[44], and the effect of grain boundary scattering on carrier mobility[45] can lead to degradation of TE performance in
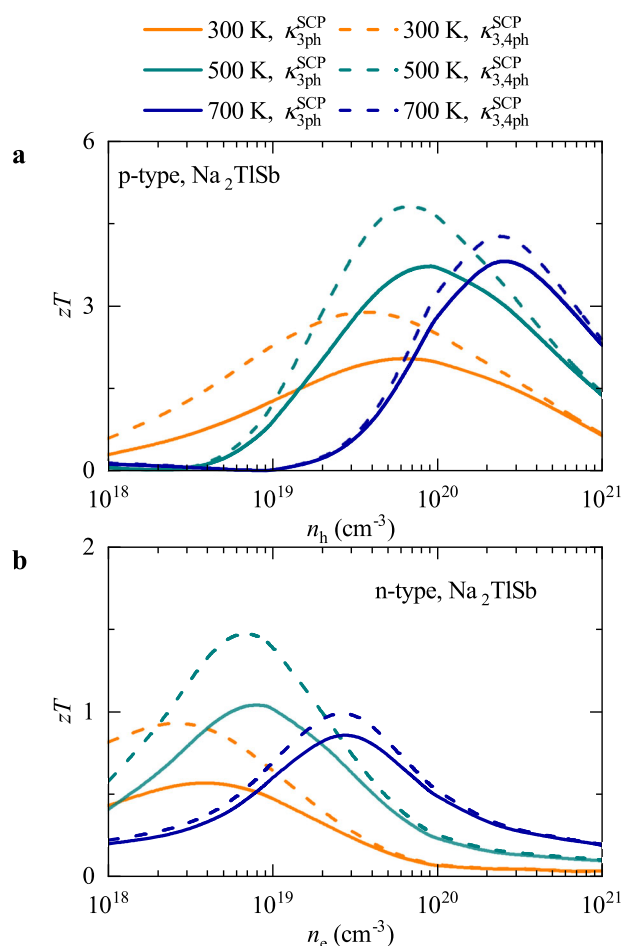
Fig. 8 TE performance. The calculated TE figure of merit with the κ_{3ph}^{SCP} and $\kappa_{3,4ph}^{SCP}$ for **a** p-type and **b** n-type Na$_2$TlSb at 300, 500, and 700 K. The SOC is also included in the calculations.

experiments. Hence, if the above factors are taken into account, the calculated zT value will be slightly lower. Moreover, we only use the BTE to compute the electronic transport properties of Na$_2$TlSb at specific doping concentrations without considering specific dopability, which also means that further experimental and theoretical explorations are required. Additionally, to determine the thermodynamic limit of achievable dopant concentrations, we estimated defect solubility for the formation of p-type and n-type semiconductors. We considered several possible neutral defects, including Na vacancy, Tl vacancy, Au in place of Tl (Au$_{Tl}$), Hg in place of Tl (Hg$_{Tl}$), and Pb in place of Tl (Pb$_{Tl}$). The calculated defect formation energy (ΔE_F^{def}) of Na (Tl) vacancy in Na$_2$TlSb is 0.10 (0.27) eV/defect in Na (Tl) poor condition. The above values are comparable to Na-doped PbTe (0.27 eV/defect)[46], where the hole doping concentration can achieve 10^{20} cm^{-3} at room temperature[41,47]. The calculations indicated that the optimum hole concentration can be obtained in Na$_2$TlSb. Furthermore, the ΔE_F^{def} of Au$_{Tl}$ (Hg$_{Tl}$) is 0.75 (0.19) eV/defect. These values suggested that Hg$_{Tl}$ is more likely to reach the optimum value of hole concentration, while Au$_{Tl}$ is difficult. Actually, since Au (Hg) are as heavy as Tl, their introduction is expected to maintain the Tl-dominated soft phonons and strong anharmonicity, thereby preserving an ultralow κ_L in p-type Na$_2$TlSb. For these reasons, the use of Au$_{Tl}$ and Hg$_{Tl}$ would be a strategic doping mechanism to best trigger p-type performance despite the toxicity of Hg and the low doping solubility of Au. Similarly, the introduction of Pb$_{Tl}$ is also expected to maintain ultralow κ_L in n-type Na$_2$TlSb. Hence, we also calculated the ΔE_F^{def}

of Pb$_{Tl}$ to be −0.18 eV/defect, which indicates that Pb$_{Tl}$ is easier to achieve the optimal doping concentration. The above results strongly indicate that the doping concentration required for optimal zT can be achieved through defects.

DISCUSSION

In summary, we investigate the thermal and TE transport properties in Na$_2$TlSb using the first-principles calculations combined with SCP theory and Boltzmann transport equations, which explicitly include the phonon frequency shift and 4ph scattering caused by quartic anharmonicity. Our results indicate that the ultralow κ_L of Na$_2$TlSb can be explained by the small v_{ph} and strong 3ph and 4ph scattering. The Tl atom with rattling behavior has strong temperature dependence and cubic and quartic anharmonicity, which plays an important role in the phonon without imaginary frequencies. Additionally, the low-frequency four-phonon scattering rates in Na$_2$TlSb can match or even exceed the three-phonon scattering rates. Meanwhile, the multi-valley band structure at VBM increases the band degeneracy, resulting in a high TE power factor in p-type Na$_2$TlSb. Additionally, due to large electronic band dispersion and remarkable band asymmetry at CBM, the n-type Na$_2$TlSb exhibit a high σ. By considering ADP, POP, and IMP scattering, we capture a rational electronic relaxation time and transport properties. As a consequence, the n-type and p-type Na$_2$TlSb show a high TE figure of merit, whose values are 1.48 and 4.81 at the optimal carrier concentration and 500 K. Our study reveals the important role of quartic anharmonicity in phonon thermal transport, which contributes to our comprehensive understandings of ultralow κ_L microscopic mechanism in full-Heusler compounds. At the same time, we also provide ideas for the rational design of high-performance TE materials.

METHODS
First-principles calculation and CSLD

We perform first-principle calculations employing the VASP code[48,49], using the plane-wave basis set and projector augmented-wave method to simulate the potentials of ions cores and valence electrons[50]. The exchange-correlational interactions is dealt by the Perdew-Burke-Ernzerhof revised for solids (PBEsol) functional[51] of the generalized gradient approximation (GGA)[52]. We use 520 eV as the kinetic energy cut-off, and Γ-centered $12 \times 12 \times 12$ **k**-point meshes to sample the whole Brillouin zone. The structure of Na$_2$TlSb is fully relaxed until the energy and Hellmann-Feynman force convergence criterion are less than 10^{-8} eV and 1×10^{-4} eV Å^{-1}, respectively. Throughout the thermal transport calculations, we consider the nonanalytic part of the dynamics matrix, which is derived using the dielectric tensor ϵ and Born effective charges Z^* calculated by the density functional perturbation theory (DFPT)[53]. All required harmonic (HA) and anharmonic interatomic force constants (IFCs) are calculated in the $2 \times 2 \times 2$ supercell with $6 \times 6 \times 6$ **k**-point meshes, implemented in the ALAMODE package[35,54]. Additionally, we also calculated the HA phonon dispersion curves within the $2 \times 2 \times 2$ and $3 \times 3 \times 3$ supercells to check the convergence of IFCs, as shown in Supplementary Fig. 4. It can be observed that the HA phonon dispersion curves agree well with each other, indicating the harmonic IFCs exacted form the $2 \times 2 \times 2$ supercell are enough to capture convergence results. Furthermore, it can be deduced that anharmonic IFCs exacted from $2 \times 2 \times 2$ supercell are also convergent, since anharmonic IFCs generally converge faster than harmonic IFCs. Specifically, the HA IFCs were extracted in three configurations produced by the finite-displacement method[55]. To obtain the displacement and force datasets required for anharmonic (cubic and quartic) IFCs, we use 4000-step ab initio

molecular dynamics (AIMD) simulation with 2 fs time step and 300 K temperature to capture 80 snapshots first. On this basis, we obtain 80 quasi-random configurations by applying the random displacement of 0.1 Å to each atom in the 80 snapshots. Finally, we extract displacement and force information obtained from 80 quasi-random configurations to derive anharmonic IFCs via the compressive sensing lattice dynamics (CSLD) method[56]. In the CSLD calculations, we consider all (third-) nearest neighbor interactions for third- (fourth- to sixth-) order IFCs. Our calculations use 80 quasi-random configurations, more than used in previous work on Tl_3VSe_4[57] and cubic $SrTiO_3$[35], are sufficient to capture accurate aharmonic IFCs that produce convergent results.

Calculation of transport properties

We calculate the temperature-dependence anharmonic phonon energy eigenvalues, including the off-diagonal elements of phonon self-energies. On top of SCP calculations, the thermal transport parameters is solved based on the phonon BTE, as employed in the FourPhonon package[58–60]. Generally, the computational cost of 4ph scattering is expensive in most materials. Hence, to ensure sufficient convergence, we use the available 4ph phase spaces as the criterion for calculating the 4ph SRs. We use $12 \times 12 \times 12$ **q**-mesh to capture the κ_L, and the numbers of available 3ph and 4ph scattering processes have reached approximately 1.8×10^6 and 1.6×10^{10}, respectively. The numbers of available 4ph scattering processes are much larger than $LiCoO_2$[60], indicating that present calculations are sufficient to obtain an accurate κ_L. Finally, we obtained the κ_L, which is defined as

$$\kappa_L = \frac{\hbar^2}{k_B T^2 V N_q} \sum_{\mathbf{q}v} n_{\mathbf{q}v}(n_{\mathbf{q}v} + 1)\omega_{\mathbf{q}v}^2 v_{\mathbf{q}v} F_{\mathbf{q}v}, \tag{2}$$

where k_B is the Boltzmann constant, $\hbar$ is the reduced Planck's constant, V is the volume of the unit cell, N_q is the number of wave vectors, $\mathbf{q}$ and v are signs of the phonon modes, $\omega_{\mathbf{q}v}$ is frequency, $v_{\mathbf{q}v}$ is the group velocity. The $F_{\mathbf{q}v}$ is defined as

$$F_{\mathbf{q}v} = \tau_{\mathbf{q}v}(v_{\mathbf{q}v} + \Delta_{\mathbf{q}v}), \tag{3}$$

where $\tau_{\mathbf{q}v}$ and $\Delta_{\mathbf{q}v}$ are the phonon lifetime of single-mode relaxation time approximation and quantity displaying the population deviation of the iterative solution. To examine the stability of Na_2TlSb at 700 K, we performed 20,000-step AIMD simulations with a time step of 2 fs.

The electronic band structure, crystal orbital Hamilton population (COHP), high-frequency dielectric constants ϵ_∞, and deformation potentials are calculated using PBEsol functional with $12 \times 12 \times 12$ **k**-point meshes. The elastic constants C_{ij}, static dielectric constants ϵ_s, and effective polar phonon frequency ω_{po} are calculated using DFPT. The above materials' parameters are listed in Supplementary Table 1. The accurate band gap is obtained using HSE06 functional and $12 \times 12 \times 12$ **k**-point meshes. The electronic band structure is recalculated in uniform $135 \times 135 \times 135$ **k**-point grids to obtain the electron relaxation time τ_e and electronic transport parameters, as performed in AMSET code[61]. Since Na_2TlSb contains a heavy Tl element, the spin-orbit coupling (SOC) is also included in the calculations of electronic transport properties. The τ_e is calculated by including the fully anisotropic acoustic deformation potential (ADP) scattering, polar optical phonon (POP) scattering, and ionized impurity (IMP) scattering. The electron-acoustic phonon and electron-optical phonon interaction is treated by ADP and POP scattering. For details of scattering rates, please refer to the Supplementary Methods.

DATA AVAILABILITY

All data were available from the corresponding authors upon reasonable request.

CODE AVAILABILITY

The related codes are available from the corresponding authors upon reasonable request.

REFERENCES

1. Sootsman, J. R., Chung, D. Y. & Kanatzidis, M. G. New and old concepts in thermoelectric materials. *Angew. Chem. Int. Ed.* **48**, 8616–8639 (2009).
2. Yue, T., Xu, B., Zhao, Y., Meng, S. & Dai, Z. Ultra-low lattice thermal conductivity and anisotropic thermoelectric transport properties in Zintl compound β-K_2Te_2. *Phys. Chem. Chem. Phys.* **24**, 4666–4673 (2022).
3. Zhao, Y. et al. High thermopower and potential thermoelectric properties of crystalline LiH and NaH. *Phys. Rev. B* **95**, 014307 (2017).
4. Liu, W. et al. Convergence of conduction bands as a means of enhancing thermoelectric performance of n-Type $Mg_2Si_{1-x}Sn_x$ solid solutions. *Phys. Rev. Lett.* **108**, 166601 (2012).
5. Wang, H., Gibbs, Z. M., Takagiwa, Y. & Snyder, G. J. Tuning bands of PbSe for better thermoelectric efficiency. *Energy Environ. Sci.* **7**, 804–811 (2014).
6. Lv, H. Y., Lu, W. J., Shao, D. F. & Sun, Y. P. Enhanced thermoelectric performance of phosphorene by strain-induced band convergence. *Phys. Rev. B* **90**, 085433 (2014).
7. Li, J. et al. The roles of Na doping in BiCuSeO oxyselenides as a thermoelectric material. *J. Mater. Chem. A* **2**, 4903–4906 (2014).
8. Kim, G.-H., Shao, L., Zhang, K. & Pipe, K. P. Engineered doping of organic semiconductors for enhanced thermoelectric efficiency. *Nat. Mater.* **12**, 719–723 (2013).
9. Hicks, L. D. & Dresselhaus, M. S. Effect of quantum-well structures on the thermoelectric figure of merit. *Phys. Rev. B* **47**, 12727–12731 (1993).
10. Parker, D., Chen, X. & Singh, D. J. High three-dimensional thermoelectric performance from low-dimensional bands. *Phys. Rev. Lett.* **110**, 146601 (2013).
11. Yue, T., Sun, Y., Zhao, Y., Meng, S. & Dai, Z. Thermoelectric performance in the binary semiconductor compound A_2Se_2 (A = K, Rb) with host-guest structure. *Phys. Rev. B* **105**, 054305 (2022).
12. Feng, Z., Fu, Y., Yan, Y., Zhang, Y. & Singh, D. J. Zintl chemistry leading to ultralow thermal conductivity, semiconducting behavior, and high thermoelectric performance of hexagonal KBaBi. *Phys. Rev. B* **103**, 224101 (2021).
13. He, J., Xia, Y., Naghavi, S. S., Ozoliņš, V. & Wolverton, C. Designing chemical analogs to pbte with intrinsic high band degeneracy and low lattice thermal conductivity. *Nat. Commun.* **10**, 719 (2019).
14. Li, Z., Xiao, C., Zhu, H. & Xie, Y. Defect chemistry for thermoelectric materials. *J. Am. Chem. Soc.* **138**, 14810–14819 (2016).
15. Hu, L., Zhu, T., Liu, X. & Zhao, X. Point defect engineering of high-performance bismuth-telluride-based thermoelectric materials. *Adv. Funct. Mater.* **24**, 5211–5218 (2014).
16. Xia, Y. & Chan, M. K. Y. Anharmonic stabilization and lattice heat transport in rocksalt β-GeTe. *Appl. Phys. Lett.* **113**, 193902 (2018).
17. Chen, Z. et al. Low lattice thermal conductivity by alloying SnTe with $AgSbTe_2$ and CaTe/MnTe. *Appl. Phys. Lett.* **115**, 073903 (2019).
18. He, J., Girard, S. N., Kanatzidis, M. G. & Dravid, V. P. Microstructure-lattice thermal conductivity correlation in nanostructured PbTe0.7S0.3 thermoelectric materials. *Adv. Funct. Mater.* **20**, 764–772 (2010).
19. Tadano, T., Gohda, Y. & Tsuneyuki, S. Impact of rattlers on thermal conductivity of a thermoelectric clathrate: a first-principles study. *Phys. Rev. Lett.* **114**, 095501 (2015).
20. Nolas, G. S., Poon, J. & Kanatzidis, M. Recent developments in bulk thermoelectric materials. *MRS Bull.* **31**, 199–205 (2006).
21. Park, J., Xia, Y. & Ozoliņš, V. High thermoelectric power factor and efficiency from a highly dispersive band in ba_2BiAu. *Phys. Rev. Appl.* **11**, 014058 (2019).
22. Wang, W. et al. Low lattice thermal conductivity and high figure of merit in n-type doped full-Heusler compounds X2YAu (X = Sr, Ba; Y = As, Sb). *Int. J. Energy Res.* **45**, 20949–20958 (2021).
23. Hu, Y., Jin, Y., Zhang, G. & Yan, Y. Electronic structure and thermoelectric properties of full Heusler compounds Ca2YZ (Y = Au, Hg; Z = As, Sb, Bi, Sn and Pb). *RSC Adv.* **10**, 28501–28508 (2020).
24. Wang, S.-F., Zhang, Z.-G., Wang, B.-T., Zhang, J.-R. & Wang, F.-W. Intrinsic ultralow lattice thermal conductivity in the full-Heusler compound Ba_2AgSb. *Phys. Rev. Appl.* **17**, 034023 (2022).
25. Zhao, Y. et al. Quartic anharmonicity and anomalous thermal conductivity in cubic antiperovskites A_3BO(A = K, Rb; B = Br, Au). *Phys. Rev. B* **101**, 184303 (2020).
26. Li, C. W. et al. Orbitally driven giant phonon anharmonicity in SnSe. *Nat. Phys.* **11**, 1063–1069 (2015).

27. Liu, H. et al. Copper ion liquid-like thermoelectrics. *Nat. Mater.* **11**, 422–425 (2012).

28. Wu, D. et al. Origin of the high performance in gete-based thermoelectric materials upon bi2te3 doping. *J. Am. Chem. Soc.* **136**, 11412–11419 (2014).

29. Zhao, Y. et al. Lattice thermal conductivity including phonon frequency shifts and scattering rates induced by quartic anharmonicity in cubic oxide and fluoride perovskites. *Phys. Rev. B* **104**, 224304 (2021).

30. Xia, Y. et al. High-throughput study of lattice thermal conductivity in binary rocksalt and zinc blende compounds including higher-order anharmonicity. *Phys. Rev. X* **10**, 041029 (2020).

31. Wu, Z.-j et al. Crystal structures and elastic properties of superhard IrN_2 and IrN_3 from first principles. *Phys. Rev. B* **76**, 054115 (2007).

32. Xia, Y., Pal, K., He, J., Ozoliņš, V. & Wolverton, C. Particlelike phonon propagation dominates ultralow lattice thermal conductivity in crystalline Tl_3VSe_4. *Phys. Rev. Lett.* **124**, 065901 (2020).

33. Tadano, T. & Tsuneyuki, S. Quartic anharmonicity of rattlers and its effect on lattice thermal conductivity of clathrates from first principles. *Phys. Rev. Lett.* **120**, 105901 (2018).

34. He, J. et al. Ultralow thermal conductivity in full Heusler semiconductors. *Phys. Rev. Lett.* **117**, 046602 (2016).

35. Tadano, T. & Tsuneyuki, S. Self-consistent phonon calculations of lattice dynamical properties in cubic $SrTiO_3$ with first-principles anharmonic force constants. *Phys. Rev. B* **92**, 054301 (2015).

36. Ravichandran, N. K. & Broido, D. Unified first-principles theory of thermal properties of insulators. *Phys. Rev. B* **98**, 085205 (2018).

37. Ravichandran, N. K. & Broido, D. Phonon-phonon interactions in strongly bonded solids: selection rules and higher-order processes. *Phys. Rev. X* **10**, 021063 (2020).

38. Markov, M., Rezaei, S. E., Sadeghi, S. N., Esfarjani, K. & Zebarjadi, M. Thermoelectric properties of semimetals. *Phys. Rev. Mater.* **3**, 095401 (2019).

39. Gong, J. J. et al. Investigation of the bipolar effect in the thermoelectric material CaMg2Bi2 using a first-principles study. *Phys. Chem. Chem. Phys.* **18**, 16566–16574 (2016).

40. Pei, Y.-L. & Liu, Y. Electrical and thermal transport properties of Pb-based chalcogenides: PbTe, PbSe, and PbS. *J. Alloys Compd.* **514**, 40–44 (2012).

41. Wang, H., Pei, Y., LaLonde, A. D. & Snyder, G. J. Heavily doped p-type PbSe with high thermoelectric performance: an alternative for PbTe. *Adv. Mater.* **23**, 1366–1370 (2011).

42. Fetherolf, J. H., Shih, P. & Berkelbach, T. C. Conductivity of an electron coupled to anharmonic phonons. arXiv:2205.09811, https://doi.org/10.48550/arXiv.2205.09811 (2022).

43. Kraemer, D. et al. High thermoelectric conversion efficiency of MgAgSb-based material with hot-pressed contacts. *Energy Environ. Sci.* **8**, 1299–1308 (2015).

44. Zhu, Q., Song, S., Zhu, H. & Ren, Z. Realizing high conversion efficiency of Mg3Sb2-based thermoelectric materials. *J. Power Sources* **414**, 393–400 (2019).

45. Hu, C., Xia, K., Fu, C., Zhao, X. & Zhu, T. Carrier grain boundary scattering in thermoelectric materials. *Energy Environ. Sci.* **15**, 1406–1422 (2022).

46. He, J. et al. Role of sodium doping in lead chalcogenide thermoelectrics. *J. Am. Chem. Soc.* **135**, 4624–4627 (2013).

47. Wang, X. et al. Sodium substitution in lead telluride. *Chem. Mater.* **30**, 1362–1372 (2018).

48. Kresse, G. & Furthmüller, J. Efficiency of ab-initio total energy calculations for metals and semiconductors using a plane-wave basis set. *Comput. Mater. Sci.* **6**, 15–50 (1996).

49. Kresse, G. & Furthmüller, J. Efficient iterative schemes for ab initio total-energy calculations using a plane-wave basis set. *Phys. Rev. B* **54**, 11169–11186 (1996).

50. Kresse, G. & Joubert, D. From ultrasoft pseudopotentials to the projector augmented-wave method. *Phys. Rev. B* **59**, 1758–1775 (1999).

51. Csonka, G. I. et al. Assessing the performance of recent density functionals for bulk solids. *Phys. Rev. B* **79**, 155107 (2009).

52. Perdew, J. P., Burke, K. & Ernzerhof, M. Generalized gradient approximation made simple. *Phys. Rev. Lett.* **77**, 3865–3868 (1996).

53. Baroni, S., de Gironcoli, S., Dal Corso, A. & Giannozzi, P. Phonons and related crystal properties from density-functional perturbation theory. *Rev. Mod. Phys.* **73**, 515–562 (2001).

54. Tadano, T., Gohda, Y. & Tsuneyuki, S. Anharmonic force constants extracted from first-principles molecular dynamics: applications to heat transfer simulations. *J. Phys. Condens. Matter* **26**, 225402 (2014).

55. Esfarjani, K. & Stokes, H. T. Method to extract anharmonic force constants from first principles calculations. *Phys. Rev. B* **77**, 144112 (2008).

56. Zhou, F., Sadigh, B., Åberg, D., Xia, Y. & Ozoliņš, V. Compressive sensing lattice dynamics. II. Efficient phonon calculations and long-range interactions. *Phys. Rev. B* **100**, 184309 (2019).

57. Zeng, Z. et al. Nonperturbative phonon scatterings and the two-channel thermal transport in Tl_3VSe_4. *Phys. Rev. B* **103**, 224307 (2021).

58. Feng, T., Lindsay, L. & Ruan, X. Four-phonon scattering significantly reduces intrinsic thermal conductivity of solids. *Phys. Rev. B* **96**, 161201 (2017).

59. Feng, T. & Ruan, X. Quantum mechanical prediction of four-phonon scattering rates and reduced thermal conductivity of solids. *Phys. Rev. B* **93**, 045202 (2016).

60. Han, Z., Yang, X., Li, W., Feng, T. & Ruan, X. FourPhonon: an extension module to ShengBTE for computing four-phonon scattering rates and thermal conductivity. *Comput. Phys. Commun.* **270**, 108179 (2022).

61. Ganose, A. M. et al. Efficient calculation of carrier scattering rates from first principles. *Nat. Commun.* **12**, 1–9 (2021).

62. Momma, K. & Izumi, F. *V*ESTA: a three-dimensional visualization system for electronic and structural analysis. *J. Appl. Crystallogr.* **41**, 653–658 (2008).

ACKNOWLEDGEMENTS

AUTHOR CONTRIBUTIONS

The research was conceived and designed by YZ and ZD. Calculations on stabilities and thermoelectric properties were conducted by TY. Analysis of the data was performed by TY, JN, and SM. Methodology and supervision, project administration is ZD. All authors discussed the results and contributed to writing the manuscript.

COMPETING INTERESTS

The authors declare no competing interests.

ADDITIONAL INFORMATION

Supplementary information The online version contains supplementary material available at https://doi.org/10.1038/s41524-023-00970-4.

Correspondence and requests for materials should be addressed to Yinchang Zhao, Jun Ni, Sheng Meng or Zhenhong Dai.

Reprints and permission information is available at http://www.nature.com/reprints

Publisher's note Springer Nature remains neutral with regard to jurisdictional claims in published maps and institutional affiliations.